

Chapter 8: Unconventional topology with a Rashba SOC quantum gas

As I mentioned in the previous Chapter topological order is present in a wide range of physical systems and is quantified by integer valued topological invariants such as the Chern number. In this Chapter I describe a system with Rashba-type spin-orbit coupling whose topological invariants can take half-integer values. If the concept of half-integer invariants does not sound odd, think of a donut with half a hole.

Ultracold atomic systems are an emerging platform for engineering topological lattices, from the Harper-Hofstadter model [96, 97], the Haldane model [98], to the Rice-Mele model [99, 100] as well as assembling spin-orbit coupled lattices without analogues in existing materials [101, 102]. However, experimental realizations of topological materials have mostly focused on engineering different topological bands (with different Berry curvatures) in lattice systems, where the BZ is always a torus. Here I show that by eliminating the lattice potential and thereby changing the BZ from \mathbb{T}^2 to \mathbb{R}^2 , i.e. from a torus to a Cartesian plane, it is possible to create topological branches of the dispersion relation with half-integer Chern number.

The experiments presented here combine the experimental techniques that were presented in Chapters 5 and 6, additionally I use the key concepts of topology described in Chapter 7. This Chapter is organized in the following way: First I give a general overview of Rashba SOC and describe theoretical proposals for engineering this type of coupling in ultracold atom systems. Then I describe our experimental implementation of Rashba SOC in the lab using a trio of Raman coupled CDD states and validate our quantum engineering using Fourier transform spectroscopy. Finally I describe a quantum state tomography procedure to measure the eigenstates of our system, from which we can directly obtain the Chern number.

To avoid confusion between dressed state xyz labels and Cartesian coordinates, in this Chapter I will use the numbers 1, 2, 3 to label the coordinates $\mathbf{e}_x, \mathbf{e}_y, \mathbf{e}_z$ and the letters x, y, z to label clock state parameters.

8.1 Rashba spin-orbit coupling

Rashba SOC [18] appears in condensed matter systems where electrons are confined in a 2D plane and experience an intrinsic out-of-plane electric field. If the electron's momentum is given by $\hbar\mathbf{k} = \hbar(k_x\mathbf{e}_x + k_y\mathbf{e}_y)$ and the electric field is $\mathbf{E} = E\mathbf{e}_z$, in the electron's moving frame there will be a momentum dependent magnetic field $\mathbf{B}_{\text{SOC}} = -\hbar\mathbf{k}/m \times \mathbf{E}/c^2 = \hbar E/mc^2(-k_y, k_x, 0)$. The interaction

between the electron's spin with this field through the magnetic Zeeman interaction $-\mu \cdot \mathbf{B}_{\text{SOC}}$ gives rise to the SOC Hamiltonian

$$\hat{H}_{\text{SOC}} = \frac{2\alpha}{m}(k_y\hat{\sigma}_x - k_x\hat{\sigma}_y) \quad (8.1)$$

where $\alpha = g\mu_B E/c^2$, g is the electrons gyromagnetic ratio, μ_B is the Bohr magneton and $\hat{\sigma}_i$ are the Pauli matrices.

As can be seen in Figure 1, the Rashba dispersion relation is characterized by having a Dirac point located at $\mathbf{k} = 0$ (see Section 7.5) and a degenerate ground state that is described by the ring $k_x^2 + k_y^2 = \alpha^2$. If we combine Equation 8.1 with the free particle Hamiltonian the Hamiltonian can be written as $\hat{H} = (\hbar\mathbf{k} - \hat{\mathbf{A}})^2/2m$ where $\hat{\mathbf{A}} = \alpha(\hat{\sigma}_y\mathbf{e}_x - \hat{\sigma}_x\mathbf{e}_y)$ can be interpreted as a (matrix valued) non-Abelian gauge potential [103] whose elements do not commute. This term is closely related to the Berry connection discussed in Section 7.3. This non-Abelian gauge potential in combination with the Dirac point hints at us that a system with Rashba SOC has non-trivial topology.

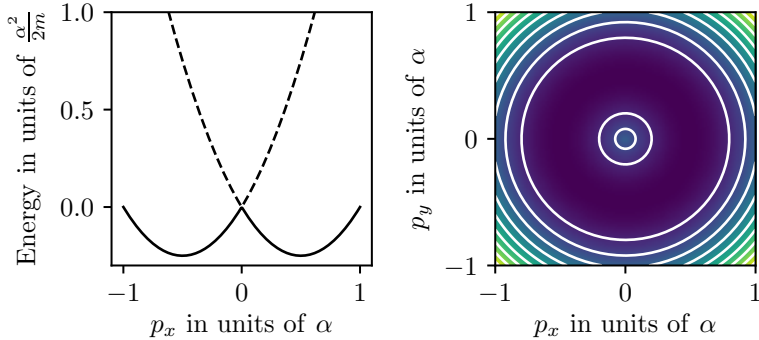


Figure 1: The Rashba dispersion relation has a Dirac point located at $\mathbf{k} = 0$ and a degenerate ground state that is described by the ring $k_x^2 + k_y^2 = \alpha^2$. [TODO: Might be nice to add the 'hedgehog' field as well]

SOC is a necessary ingredient for realizing \mathbb{Z}_2 topological insulators and the quantum spin-Hall effect. Furthermore, the degeneracy of the ground state single particle eigenstates could open the possibility of studying strongly correlated phases in the presence of interactions for systems of both fermions and bosons [104–106]. Using ultracold atomic systems to engineer SOC, and in particular Rashba type SOC, has been a longstanding goal [20].

8.2 Rashba SOC for neutral atoms

Proposals for engineering Rashba type SOC in neutral atoms consist in using lasers to link internal states of an atom with its linear momentum. In order to achieve

non-trivial gauge potentials it is necessary to couple $N \geq 3$ levels (see [107]). I will describe the proposal by [108] which considers a ‘ring coupling’ which is shown in Figure 2 for the case of $N = 3$. The states $|j\rangle$ represent internal atomic states and they are linked to each other with complex valued matrix elements $\frac{\Omega_j}{2} e^{i\mathbf{k}_j \cdot \mathbf{x}}$, where \mathbf{k}_j is a momentum transfer associated with the $|j\rangle \rightarrow |j+1\rangle$ transition and $\Omega_i = e^{i\phi_i} |\Omega|$ represents the coupling strength. We require that $\sum \mathbf{k}_i = 0$ so that no momentum is transferred when a closed loop $|1\rangle \rightarrow |2\rangle \dots \rightarrow |N\rangle \rightarrow |1\rangle$ is completed. For this case the \mathbf{k}_i momenta vectors can be written as $\mathbf{k}_j = \mathbf{K}_{j+1} - \mathbf{K}_j$, and we make $\mathbf{K}_j = k_L \sin(2\pi j/N) \mathbf{e}_x + k_L \cos(2\pi j/N) \mathbf{e}_y$, corresponding to the vertices of an N sided regular polygon. We can further make a gauge transformation such that we can replace the phases ϕ_i associated to each coupling with $\bar{\phi} = \sum_i \phi_i / N$.

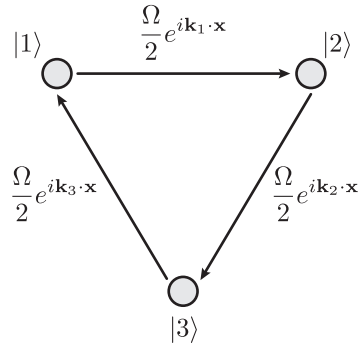


Figure 2: The Rashba ring coupling. To generate Rashba SOC in a system of cold atoms it is necessary to cyclically couple $N \geq 3$ internal states such that the transition $|j\rangle \rightarrow |j+1\rangle$ has a momentum transfer \mathbf{k}_j and $\sum_j \mathbf{k}_j = 0$ such that there is no momentum transfer for a closed loop $|1\rangle \rightarrow |2\rangle \dots |N\rangle \rightarrow |1\rangle$. The ring coupling combined with the free particle Hamiltonian give rise to a 2-level subspace that can be described to first order by the Rashba Hamiltonian

The Hamiltonian describing this coupling along with the kinetic term is

$$H_{j,j'} = \frac{\hbar^2 k^2}{2m} \delta_{j,j'} + \frac{\Omega}{2} (e^{i(\bar{\phi} + \mathbf{k}_j \cdot \mathbf{x})} \delta_{j,j'+1} + \text{h.c.}), \quad (8.2)$$

and after applying the unitary transformation $U_{j,j'} = \exp[i\mathbf{K}_i \cdot \mathbf{x}] \delta_{j,j'}$ ¹ it gets transformed to

$$H_{j,j'} = \frac{\hbar^2}{2m} |\mathbf{q} + \mathbf{K}_j|^2 \delta_{j,j'} + \frac{\Omega}{2} (e^{i\bar{\phi}} \delta_{j,j'+1} + \text{h.c.}), \quad (8.3)$$

where I have replaced the momentum \mathbf{k} by the quasimomentum \mathbf{q} . The off diagonal terms of Equation 8.3 can be related to a 1D periodic tight-binding Hamiltonian with hopping elements $\Omega/2$ where the internal states $|j\rangle$ represent lattice sites and completing one loop corresponds to gaining a ‘flux’ of $N\bar{\phi}$. To visualize how the

¹This transformation is equivalent to applying a state dependent momentum boost $\mathbf{k} \rightarrow \mathbf{k} + \mathbf{K}_j$

Rashba Hamiltonian emerges from this coupling scheme, it is helpful to write the Hamiltonian in a basis that is conjugate to the index j ²

$$|l\rangle = \frac{1}{\sqrt{N}} \sum_{j=1}^N e^{i2\pi jl/N} |j\rangle \quad (8.4)$$

where the index l is analogous to the crystal momentum index for a Bloch Hamiltonian. In this new basis, terms in the diagonals are displaced to the off-diagonal and likewise terms in the off diagonals are displaced to the diagonal. Under this basis the Hamiltonian starts looking very much Rashba-like

$$H_{l,l'} = \left[\frac{\hbar^2}{2m} (q^2 + k_L^2) + E_l \right] \delta_{l,l'} + \frac{\hbar^2 k_L}{m} [(iq_x + q_y)\delta_{l-1,l'} + \text{h.c}], \quad (8.5)$$

where $E_L = 2\hbar\Omega \cos(2\pi l/3 + \bar{\phi})$ correspond to the eigenenergies when $q = 0$. The phase $\bar{\phi}$ can be tuned such that a pair of states with consecutive l index become degenerate, indicating the presence of a Dirac point at $q = 0$. Figure 3 shows the energies E_l for $N = 3$ and $\bar{\phi} = 0$.

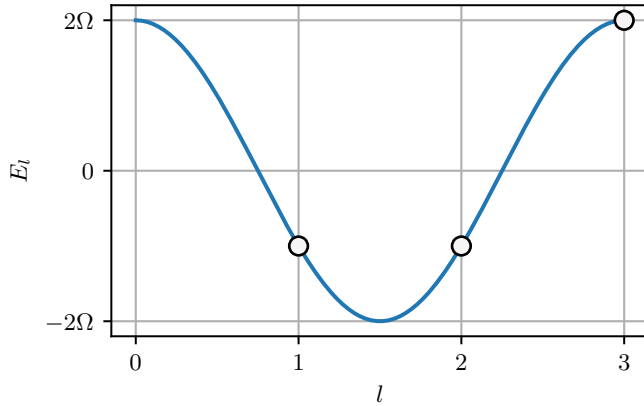


Figure 3: Eigenenergies of Equation 8.5 for $q = 0$ for $N = 3$ and $\bar{\phi} = 0$. For this particular choice of phase, the energies of the $l = 1$ and $l = 2$ states become degenerate

We can consider the degenerate states as pseudospins which are described to zeroth order by the Rashba plus free particle Hamiltonian

$$\hat{H}^{(0)} = \frac{\hbar^2 q^2}{2m} + \frac{\hbar^2 k_L}{m} (\hat{\sigma}_x q_y - \hat{\sigma}_y q_x), \quad (8.6)$$

²Just like position and momentum are conjugate variables related by Fourier transforms, the $|j\rangle$ and $|l\rangle$ basis are related by a discrete Fourier transform.

with spin orbit coupling strength given by $\alpha = \hbar^2 k_L / 2$. The zeroth-order Hamiltonian has continuous rotational symmetry while the proposed ring coupling only has discrete rotational symmetry. The symmetry of the Hamiltonian is recovered when higher order corrections are added to the Hamiltonian. The complete expressions for the higher order terms for $N = 3$ and $N = 4$ can be found in [108], and they are reminiscent of quadratic and cubic Dresselhaus SOC [109]. The largest leading order term for the $N = 3$ case is inversely proportional to Ω so that this ring-coupling scheme results in a more ‘Rashba-like’ Hamiltonian as one goes to higher coupling strengths. Figure 4 shows level curves of the ground state eigenenergies of Equation 8.5 for $N = 3$ and $\bar{\phi} = 0$ for increasing Ω . At low Ω the dispersion has discrete rotational symmetry and is characterized by three local minima³. As Ω is increased the local minima start merging into each other and in the large Ω limit we recover the characteristic Rashba ring-like dispersion.

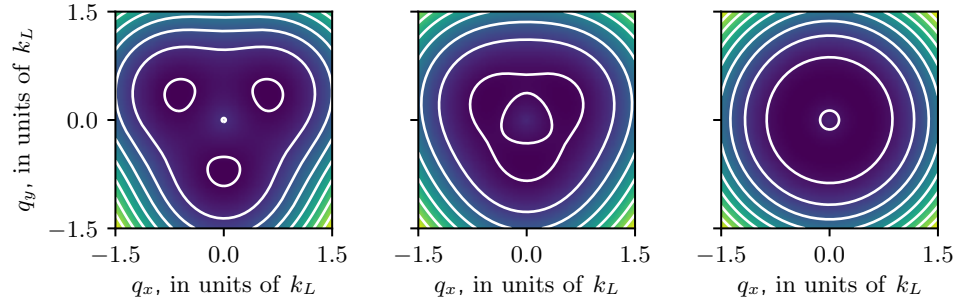


Figure 4: Ground state dispersion relation of Equation 8.5 for $N = 3$ and $\bar{\phi} = 0$ for $\Omega = 1.75 E_L$ (left), $\Omega = 3.5 E_L$ (middle) and $\Omega = 175 E_L$ (right). Higher order corrections to $\hat{H}^{(0)}$ decay as $1/\Omega^2$ and in the large Ω limit we recover the Rashba ring dispersion.

8.3 Experimental implementation of Rashba SOC

We implemented the ring-coupling scheme and thereby engineered Rashba SOC by resonantly coupling the $|xyz\rangle$ states from Chapter 6 states using two-photon Raman transitions [46] as depicted in Figure 5. The engineered system consisted of an effective spin-1/2 Rashba subspace, along with a topologically trivial high-energy branch. Our engineered Rashba system had a single Dirac cone near $\mathbf{q} = 0$, where the two lower dispersion branches become degenerate and the Berry curvature becomes singular. Each of these branches extend to infinite momentum, making the supporting manifold a plane rather than a torus. We characterized this system using both spectroscopy and quantum state tomography. This allowed us to measure the dispersion branches and directly observe the single Dirac point linking the lowest

³An alien face?

two branches as well as to reconstruct the Berry connection to derive the associated Chern numbers.

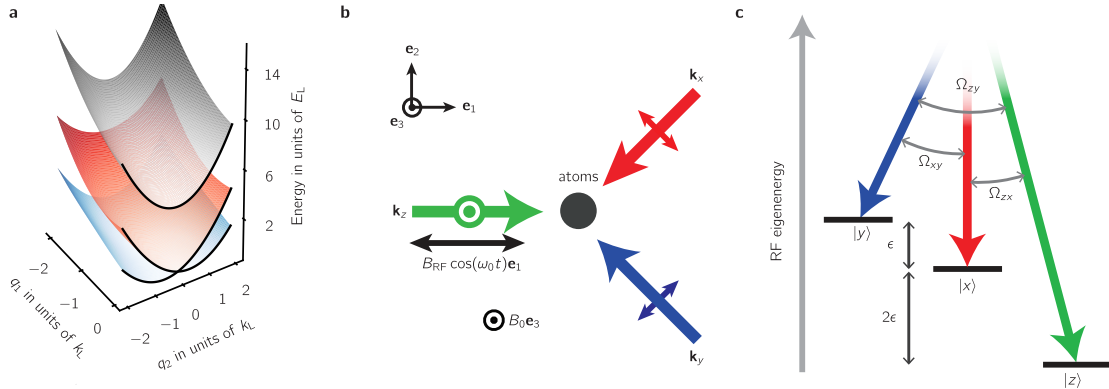


Figure 5: **a** Our engineered dispersion consisted of a two-level Rashba subspace (red and blue) with a single Dirac point linking the lowest two branches and a topologically trivial higher branch (gray). **b** We generated $|xyz\rangle$ states by combining a bias magnetic field along \mathbf{e}_3 with an RF magnetic field oscillating along \mathbf{e}_1 . These states were coupled by three cross-polarized Raman laser beams propagating along \mathbf{e}_1 , $\mathbf{e}_2 - \mathbf{e}_1$ and $-\mathbf{e}_1 - \mathbf{e}_2$. **c** Each pair of Raman lasers was in two-photon resonance with a single transition between the $|xyz\rangle$ states which we coupled strengths $(\Omega_{zx}, \Omega_{xy}, \Omega_{yz})/2\pi = (12.6(5), 8.7(8), 10(1))$ kHz.

All of our experiments started with about $N \approx 1 \times 10^{687}$ Rb atoms in a crossed optical dipole trap [110], with frequencies $(f_1, f_2, f_3) \approx (70, 85, 254)$ Hz, just above the transition temperature for Bose-Einstein condensation. We initially prepared the atoms in the $|F = 1, m_F = -1\rangle$ state of the $5S_{1/2}$ electronic ground state and transferred atoms to the $m_F = 0$ and $m_F = +1$ states as needed using ARP. A bias field $B_0 \mathbf{e}_3$ gave a $\omega_0/2\pi = 23.9$ MHz Larmor frequency along with a quadratic shift of $\epsilon/2\pi = 83.24$ kHz. The RF field used to generate the $|xyz\rangle$ states and implementing CDD had strength $\Omega_{RF} = 1.41(2)\epsilon$. We adiabatically prepared the $|xyz\rangle$ states starting from the m_F states following the procedure described in Section 6.4.

8.3.1 Raman coupling the $|xyz\rangle$ states

We Raman-coupled atoms prepared in any of the $|xyz\rangle$ states using the three cross-polarized Raman laser beams shown in Figure 5b, tuned to the ‘magic zero’ wavelength $\lambda_L = 790$ nm. We arranged the Raman lasers into the tripod configuration shown in Figure 5c, bringing each pair into two-photon resonance with a single transition with strengths $(\Omega_{zx}, \Omega_{xy}, \Omega_{yz})/2\pi = (12.6(5), 8.7(8), 10(1))$ kHz. The geometry of our experimental implementation differs from [46] where all Raman lasers are perpendicular. We had to go away from the ideal configuration because we

needed all of the Raman recoil vectors to lie on the imaging plane (spanned by \mathbf{e}_1 and \mathbf{e}_2) in order to image all the Raman induced \mathbf{k} dependent dynamics. As a result of this the dispersion relation no longer has discrete rotational symmetry, however the Dirac point is still present in our system. The only way to break the degeneracy of this system is to change the phase $\bar{\phi}$ and for our laser configuration we always have $\bar{\phi} = 0$.

The energies of the $|xyz\rangle$ states are $\omega_x = 0$ and $\omega_{z,y} = -(\epsilon \pm \sqrt{4\Omega_{\text{RF}}^2 + \epsilon^2})/2$. We set the frequencies of the Raman lasers to $\omega_x = \omega_L + \omega_0 + \omega_{xy}$, $\omega_y = \omega_L + \omega_0$ and $\omega_z = \omega_L - \omega_{zx}$, where $\omega_L = 2\pi c/\lambda_L$ and $(\omega_{zx}, \omega_{xy}, \omega_{zy})/2\pi = (166.47, 83.24, 249.71)$ kHz are the transition frequencies between pairs of dressed states and are integer multiples of ϵ for our coupling strength $\Omega = \sqrt{2}\epsilon$.

The Raman coupled states can be described by the combined kinetic and light-matter Hamiltonian

$$\hat{H}_{\text{R}}(\mathbf{k}) = \sum_{j \in \{xyz\}} \left(\frac{\hbar^2 k^2}{2m} + \hbar\omega_i \right) |j\rangle \langle j| + \sum_{j' \neq j} \hbar\Omega_{j,j'} e^{i(\mathbf{k}_{j,j'} \cdot \mathbf{x} - i\omega_{j,j'} t)} |j\rangle \langle j'|, \quad (8.7)$$

where $\mathbf{k}_{j,j'}$ is the recoil momentum from an $|j\rangle \rightarrow |j'\rangle$ transition and Ω_{ij} is the Raman coupling strength between a pair of RF dressed states. The Hamiltonian above only includes the matrix elements associated to resonant couplings. We apply the unitary transformation $\hat{U}_{j,j'} = \exp(-i\mathbf{k}_j \cdot \mathbf{x} - \omega_j t)\delta_{j,j'} |j\rangle \langle j'|$ so that the Hamiltonian takes the familiar form of the ring coupling scheme

$$\hat{H}_{\text{R}} = \sum_{j \in \{xyz\}} \left(\frac{\hbar^2(\mathbf{q} - \mathbf{k}_j)^2}{2m} + \hbar\delta_j \right) |j\rangle \langle j| + \sum_{j \neq j'} \hbar\Omega_{jj'} |j\rangle \langle j'|, \quad (8.8)$$

where \mathbf{k}_j are the Raman wave vectors and δ_j is the detuning from Raman resonance.

This coupling scheme simultaneously overcomes three limitations of earlier experiments [111, 112] that performed the ring coupling using states in both $5S_{1/2}$ hyperfine manifolds of ${}^{40}\text{K}$: (1) working in the same hyperfine manifold eliminates spin-relaxation collisions [113]; (2) unlike m_F states, the $|xyz\rangle$ states can be tripod-coupled with lasers far detuned relative to the excited state hyperfine splitting greatly reducing spontaneous emission [70]; and (3) CDD renders the $|xyz\rangle$ states nearly immune to magnetic field noise.

8.3.1.1 Floquet and off resonant coupling effects

We operated in a regime where the transition energies between the $|xyz\rangle$ states were integer multiples of ω_{xy} : $\omega_{zx} = 2\omega_{xy}$ and $\omega_{zy} = 3\omega_{xy}$, and therefore we can use Floquet theory for a complete description of our system [114]. We observed that the effective Raman coupling strengths for the driven three level system differed from our calibrations which were performed looking at Rabi oscillations from individual pairs of lasers because of the presence of nearby quasi-energy manifolds and off resonant coupling terms. This effect could be mitigated for larger values of ω_{xy} as the spacing between quasi-energy manifolds is increased and the off resonant coupling terms less

relevant. Appendix ?? has a full derivation of the Raman Hamiltonian starting from the $|m_F\rangle$ basis in the lab frame including the full time dependence and off resonant coupling terms.

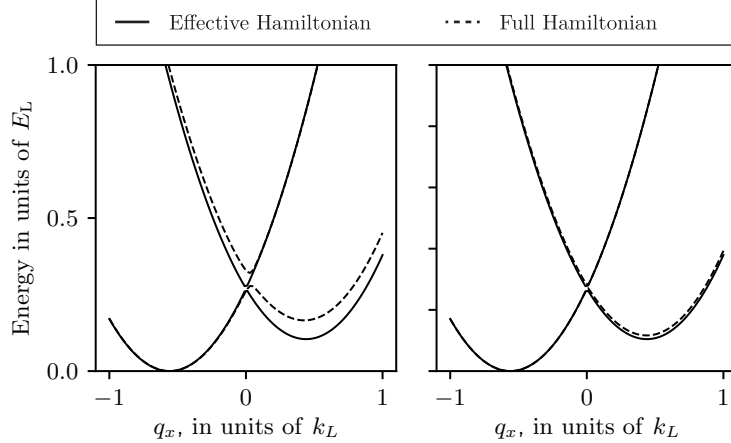


Figure 6: Solid lines: Dispersion relation from RWA Hamiltonian (Equation 8.8) as a function of q_x for $\Omega_{i,j} = 1.5 E_L$ and $\delta_i = 0$. Dashed lines: Dispersion relation computed for the full Floquet Hamiltonian. We considered $\omega_{zx} = 2\omega_{xy}$ and $\omega_{zy} = 3\omega_{xy}$ in both cases so the separation between Floquet manifolds is ω_{xy} . In the left panel $\omega_{xy} = 83.24$ kHz as in our experiments and in the right panel $\omega_{xy} = 416.2$ kHz. As the spacing between Floquet manifolds becomes we get a better agreement between the spectra of the RWA and Floquet Hamiltonians.

8.3.1.2 Lifetime

The limited lifetime due to spontaneous emission has always been a concern for Raman coupled systems. This was in part one of the reasons why we pursued the topology direction rather than trying to measure a fragile many-body phase. The measured spontaneous emission limited lifetime of our system was 320(17) ms, measured with the Raman lasers applied to the $|m_f\rangle$ states. However, it was reduced to 40(2) ms when we Raman coupled the $|xyz\rangle$ states, which we attribute to technical noise in the relative phase between the RF dressing field and the Raman laser fields, which has caused considerable consternation in ongoing experiments. All the experiments reported here were short compared to this timescale so this decreased lifetime was not an issue but it is a limitation that needs to be addressed in future experiments. Figure 7 shows measurements of the lifetimes of Raman dressed atoms in both $|m_f\rangle$ and $|xyz\rangle$ states. We obtained the lifetime by fitting decaying exponentials to the integrated OD obtained from absorption images of thermal atoms where the Raman was turned on in 1 ms and held on for up to 50 μ s⁴.

⁴How long we could hold on the Raman was limited by the RF antenna heating up.

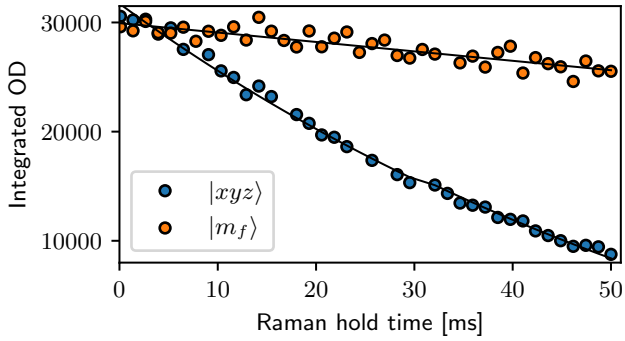


Figure 7: Lifetime of Raman dressed states. We Raman dressed atoms in the $|m_f\rangle$ and $|xyz\rangle$ states. The orange markers correspond to atoms initially prepared in $|m_f = -1\rangle$ (no high power RF involved) and the blue markers correspond to atoms $|xyz\rangle$ (three averaged traces). The lifetime of doubly dressed states is significantly reduced as compared to the lifetime of the Raman dressed $|m_f\rangle$ states, indicating that resonant scattering of photons is not our only loss mechanism.

8.3.2 Measuring quasimomentum distributions

Each pair of Raman lasers coupled states $|i, \mathbf{k}\rangle \rightarrow |j, \mathbf{k} + \mathbf{k}_{i,j}\rangle$ where $|i\rangle$ and $|j\rangle$ denote the initial and final $|xyz\rangle$ states, \mathbf{k} is the initial momentum and $\mathbf{k}_{i,j} = \mathbf{k}_i - \mathbf{k}_j$ is the two-photon Raman recoil momentum. Dressed states with quasimomentum \mathbf{q} are comprised of three bare states $|j, \mathbf{k}\rangle$ with momentum $\mathbf{k} = \mathbf{q} - \mathbf{k}_j$. The eigenstates of our Rashba SOC Hamiltonian take the form

$$|\Psi_n(\mathbf{q})\rangle = \sum_{j \in xyz} \sqrt{a_{n,j}(\mathbf{q})} e^{i\phi_{n,j}(\mathbf{q})} |j, \mathbf{k} = \mathbf{q} - \mathbf{k}_j\rangle, \quad (8.9)$$

where the quasimomentum \mathbf{q} is a good quantum number and the amplitudes are parametrized by $a_{n,j}(\mathbf{q})$ and $\phi_{n,j}(\mathbf{q})$. We leveraged the wide momentum distribution of a non-condensed ensemble ($T \approx 180$ nK and $T/T_c \approx 1.1$) to sample a wide range of momentum states simultaneously. By starting separately in each of the $|xyz\rangle$ states we sampled the range of quasimomentum states shown in Figure 8b, where the momentum distributions of an initial state $|j, \mathbf{k}\rangle$ is shifted from $\mathbf{q} = 0$ by the corresponding Raman wave vector \mathbf{k}_j .

Our measurement protocol consisted of abruptly removing the confining potential and the Raman lasers, initiating a 21 ms TOF. During this TOF we adiabatically transformed each of the $|xyz\rangle$ states back to a corresponding $|m_F\rangle$ state following the procedure described in Section 6.4 and spatially separated them using a Stern-Gerlach gradient. Finally we used resonant absorption imaging to measure the resulting spin-momentum distributions.

The FWHM of the cloud after TOF is about $700 \mu\text{m}$ which is much larger than the size of the in-situ cloud $\sim 50 \mu\text{m}$ and therefore the spatial density distribution

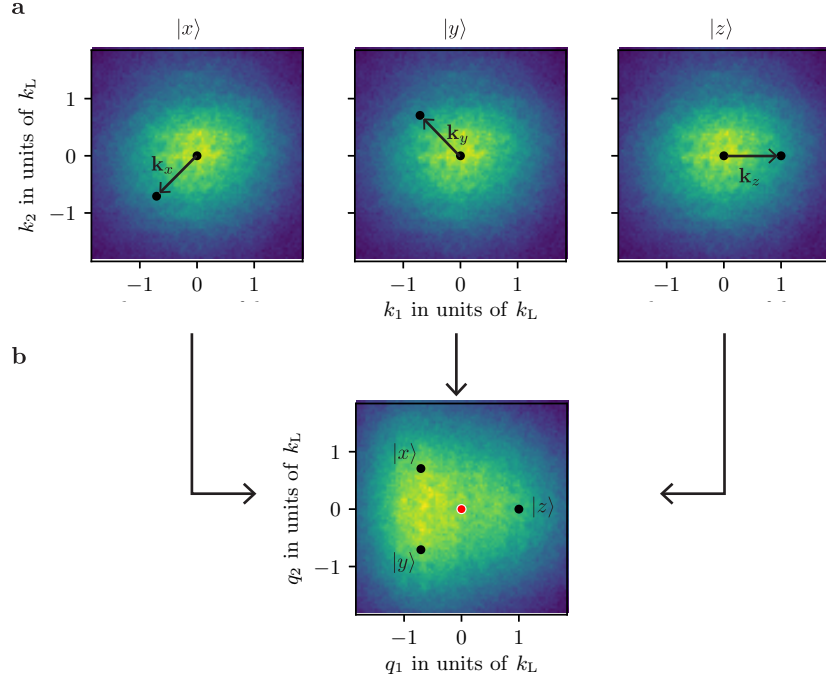


Figure 8: Mapping momentum into quasimomentum: **a** We used non-condensed atoms with a broad momentum distribution ($T \approx 180$ nK and $T/T_c \approx 1.1$). **b** Atoms in $|j, \mathbf{k}\rangle$ are mapped to Raman dressed states with quasimomentum $\mathbf{q} = \mathbf{k} + \mathbf{k}_j$. The black dots in the bottom panel represent the location of $\mathbf{k} = 0$ for each of the $|xyz\rangle$ states and the red dot corresponds to $\mathbf{q} = 0$. We performed our experiments starting separately in each of the $|xyz\rangle$ states, which allowed us to sample a larger range of quasimomentum states.

of the TOF images represents momentum distribution of the atoms. For the $7.4\text{ }\mu\text{m}$ pixel size of our camera and the 3.283 magnification of our imaging system, the momentum resolution of our images was $0.018\text{ }k_L$ and the momentum distribution of a single state measured after TOF had a FWHM of $\sim 2.2\text{ }k_L$.

8.3.2.1 Correcting shears from Stern-Gerlach gradient

The magnetic field gradient used to separate the different m_f states in TOF additionally creates a trap for atoms in the direction perpendicular to the Stern-Gerlach separation, causing a compression (expansion) of the $m_f = -1$ (+1) states (see Section 3.2.1). The faster moving atoms are subject to a stronger potential and therefore the projections of a given momentum state \mathbf{k} along the Stern-Gerlach axis and perpendicular to it were transformed as $k_{\parallel} \rightarrow k_{\parallel}$ and $k_{\perp} \rightarrow (1 + \alpha)k_{\perp}$, where $\alpha = 0$ for $m_f = 0$ and $\text{sign}(\alpha) = \pm 1$ for $m_f = \pm 1$.

Since we were interested in mapping the momentum distribution of atoms it was important for us to quantify and correct the effect of these shears in the TOF

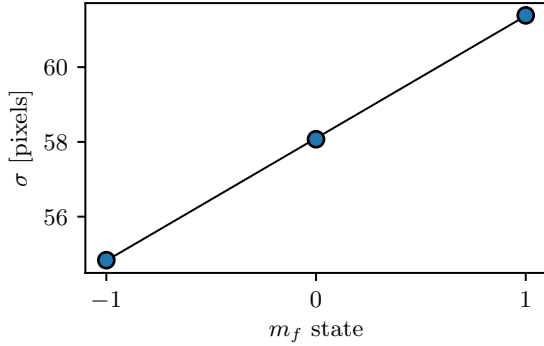


Figure 9: We measured the standard deviation of the momentum distribution along the axis perpendicular to the SG for 10 shots on each m_f state. From the slope of the linear fit we obtain a shearing parameter $\alpha \approx \pm 0.067$ for $m_f = \pm 1$.

images. We used two different methods: First we prepared thermal atoms in all three of the m_f states and fit 2D Gaussians rotated by the angle of the SG displacement; 63.8 degrees for our images. Figure 9 shows the standard deviation extracted from the Gaussian fits along the axis perpendicular to the SG deviation as a function of m_f state. We performed a linear fit of σ and found that the $m_f = \pm$ states are expanded/contracted by about $\pm 6.7\%$ size of the compared to the $m_f = 0$ cloud ($\alpha = \pm 0.067$).

Alternatively we performed the Ramsey interferometer described in Section 8.5 but coupling only 2 states, either $|z\rangle \leftrightarrow |x\rangle$ or $|x\rangle \leftrightarrow |y\rangle$ (mapped to $| -1 \rangle \leftrightarrow | 0 \rangle$ and $| 0 \rangle \leftrightarrow | +1 \rangle$ after TOF). We looked at the oscillation frequencies of the density for each pixel of the CCD camera (each sheared momentum state) and fit them to Equation 8.17 for fixed value of the recoil momentum $\mathbf{k}_{i,j}$ and with a free shear parameter that modifies \mathbf{q} . Using this method we extracted a shearing of the order of 7%, in good agreement with the Gaussian fitting method.

The transformed momentum coordinates were described by a function

$$g(\mathbf{k}) = (k_{\parallel}, (1 + \alpha)k_{\perp}) \quad (8.10)$$

and our observed data $(y_i^{(\text{shear})}, \mathbf{k}^{(\text{shear})})$ was the density in the sheared coordinate system at the i th pixel of the CCD sensor. The density in the unsheared coordinate was estimated using

$$y_j = \frac{\sum_i \exp[-(g(\mathbf{k}_j) - \mathbf{k}_i^{(\text{shear})})^2/2\sigma^2] y_i^{(\text{shear})}}{\sum_i \exp[-(g(\mathbf{k}_j) - \mathbf{k}_i^{(\text{shear})})^2/2\sigma^2]}, \quad (8.11)$$

where σ is the spacing between two consecutive pixels ($\sim 0.018 k_L$). Prior to any data analysis we applied this transformation to all of our images, where we used different values of α that define $g(\mathbf{k})$ for each of the m_f states.

8.4 Fourier spectroscopy of the Rashba dispersion

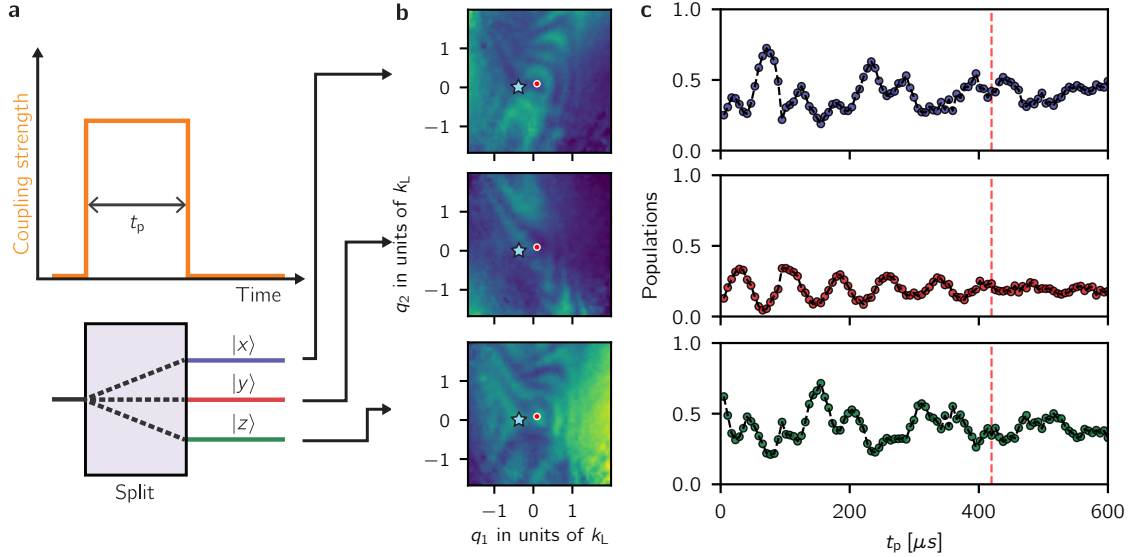


Figure 10: **a** Fourier spectroscopy protocol. We applied the Raman lasers for a variable time t_p : a Rabi-type atomic interferometer analogous to a three-port beam splitter. **b** Probabilities as a function of quasimomentum for a fixed Raman pulse time $t_p = 420 \mu s$ **c** Dynamics of the final populations of the $|xyz\rangle$ states with quasimomentum $(q_1, q_2) = (-0.55, -0.18) k_L$ (blue star in panels **b**) after initializing the system in the $|z\rangle$ state.

We directly measured the 2D dispersion relation using Fourier transform spectroscopy [40]. We considered the evolution of an initial state $|i, \mathbf{k}\rangle$ suddenly subjected to the Raman coupling lasers. This atomic Rabi-type interferometer is analogous to the three-port beam-splitter depicted in Figure 10a. During a pulse time t_p we followed the dynamics of the populations in the $|xyz\rangle$ states which evolved with oscillatory components proportional to $\sum_{j \neq n} a_{n,j}(\mathbf{q}) \cos([E_n(\mathbf{q}) - E_j(\mathbf{q})]t_p/\hbar)$, with frequencies determined by the eigenenergy differences $E_n - E_j$. Figure 10b shows the momentum dependent populations for a fixed pulse time t_p and Figure 10c shows representative final populations as a function of t_p for a fixed quasimomentum state. We Fourier transformed the populations with respect to t_p and for a given quasimomentum state for a total of 9 state, all of them with the same \mathbf{q} accounting for each of the three initial $|xyz\rangle$ states that was then split into 3 states. Figure 11 shows the PSD computed for each of the 9 states for planes of constant q_1 . The amplitude of the oscillatory components depends on the overlap integral between the initial state and the Raman dressed states (see Equation 5.1) so sampling all these states gave us access to a wider range of measurable frequencies. The spectral maps in Figure 12b were produced by averaging the PSDs from the 9 different states using

\bar{n} , the mean population in t_p , as a weight:

$$\text{PSD}^{(\text{mean})}(\mathbf{q}) = \frac{\sum_{i,j} \text{PSD}_{i,j}(\mathbf{q}) \bar{n}_{i,j}(\mathbf{q})}{\sum_{i,j} \bar{n}_{i,j}(\mathbf{q})}, \quad (8.12)$$

where the indices i, j represent the different states of the grid shown in Figure 11. The extrema in the spectral maps are the energy differences $E_n - E_j$ in the engineered dispersion (Figure 10a). Figure 12 was obtained by combining all the spectral maps, and together they show the presence of a single Dirac point in the Rashba subspace, evidenced by the gap closing near $\mathbf{q} = 0$ and the photon-like lower branch. The dashed curves correspond to the energy differences computed for our system using the dispersions shown in Figure 12a, and are in clear agreement with our experiment. This measurement directly confirms the expected set of energies, including the existence of a two-state subspace approximately described by the Rashba Hamiltonian.

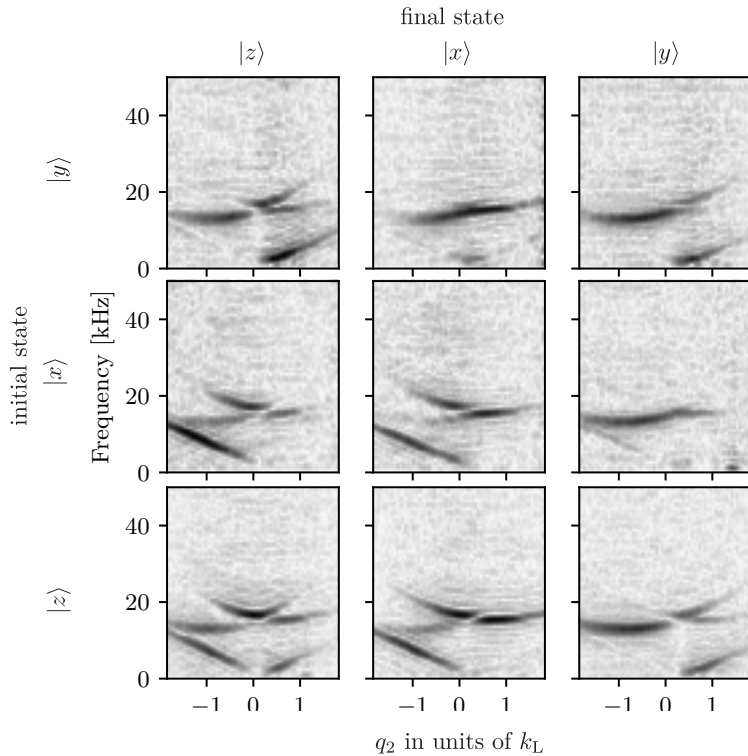


Figure 11: PSD of all the analyzed states as a function of q_2 for fixed $q_1 = 0.18 k_L$. The different overlaps between the initial state, the Raman dressed states and the measured final state result in peaks with different amplitudes.

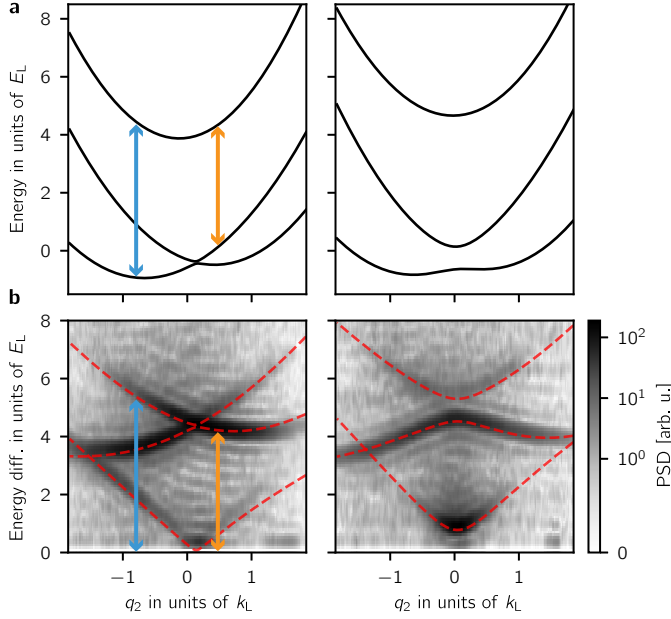


Figure 12: **a** Predicted dispersion relation as a function of q_2 for fixed $q_1 = -0.09 k_L$ (left) and $0.65 k_L$ (right), computed for the experiment parameters. The energy differences between the branches enclosing the vertical arrows appear as peaks in the spectral maps below. **b** Power spectral density (PSD) for the same parameters as above which we obtained by Fourier transforming the populations in the $|xyz\rangle$ states with respect to t_p . The dashed lines correspond to the energy differences computed using the dispersion curves on the top panel.

8.5 Quantum state tomography with Ramsey interferometer

The Fourier spectroscopy measurement confirmed our quantum engineering of the Rashba Hamiltonian. However, the energies shed no light on the topology of the different branches of the dispersion, which instead requires knowledge of the eigenstates. The Berry curvature present in the definition of the Chern number (Equation 7.11) can be derived from the Berry's connection $\mathbf{A}_n(\mathbf{q}) = i \langle \Psi_n(\mathbf{q}) | \nabla_q | \Psi_n(\mathbf{q}) \rangle$, which as discussed in Chapter 7 behaves much like a vector potential in classical electromagnetism. The Berry curvature $\Omega_n(\mathbf{q}) = \nabla_q \times \mathbf{A}(\mathbf{q})$ is the associated magnetic field and the flux through any surface is the line integral of $\mathbf{A}(\mathbf{q})$ along its boundary, after neglecting the contributions of Dirac strings which I will discuss later. Using the expression for the Raman dressed eigenstates from Equation 8.9 we obtain

$$\mathbf{A}_n(\mathbf{q}) = - \sum_{j \in \{x,y,z\}} a_{n,j}(\mathbf{q}) \nabla_q \phi_{n,j}(\mathbf{q}), \quad (8.13)$$

which depends on both the phase and amplitude of the wave function. We obtained $a_{n,j}(\mathbf{q})$ and $\phi_{n,j}(\mathbf{q})$ using a three-arm time-domain Ramsey interferometer (see Section 3.5.2), implementing a variant of quantum state tomography [115, 116]. The

use of a multi-path interferometer allowed us to transduce information about phases into state populations, which we readily obtained from absorption images.

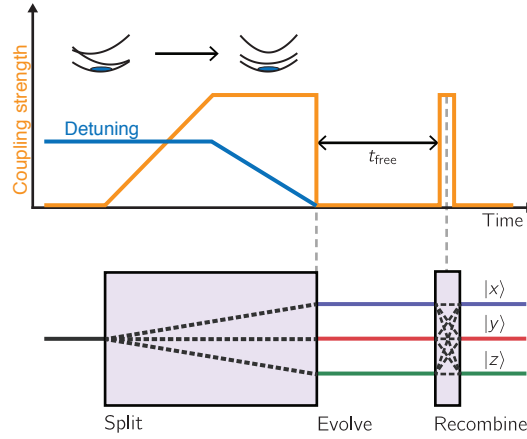


Figure 13: Experimental protocol for three-arm Ramsey interferometer (not to scale). (Top) We started with atoms in state $|z, y, \mathbf{q}_i = \mathbf{k} + \mathbf{k}_j\rangle$ and with detuning $\delta_y = \pm 5 E_L$ and $\delta_z = \pm 5 E_L$. We ramped the Raman lasers on in $750 \mu\text{s}$ and then ramped the detuning to nominally zero. We let the system evolve in the dark for times between $5 \mu\text{s}$ and $400 \mu\text{s}$, followed by a $25 \mu\text{s}$ Raman pulse. (Bottom) The implemented experimental protocol was equivalent to a three-arm interferometer that split an initial state into three final states with amplitudes related to the initial wave function phases.

Figure 13 shows our experimental protocol which I will describe in more detail in the following section. We adiabatically mapped an initial $|j, \mathbf{k}\rangle$ state into a corresponding eigenstate $|n, \mathbf{q} = \mathbf{k} + \mathbf{k}_j\rangle$, either in the topologically trivial highest dispersion branch ($n = 3$) or in the topological ground branch ($n = 1$) by dynamically tailoring both the Raman coupling strength and detuning. We suddenly turned off the Raman coupling, thereby allowing the three bare state components of the Rashba eigenstates to undergo free evolution for a time t_{free} , constituting the three arms of our time-domain interferometer. Finally we applied a three-port beam splitter using a brief Raman ‘recombination’ pulse to interfere the three arms.

8.5.1 Wave function evolution in Ramsey interferometer

Rashba dressed state preparation: We started with $|xyz\rangle$ states at different RF coupling strength $\Omega_0 = \Omega_{\text{RF}}/\pi 2 \pm 20 \text{ kHz}$, such that the energies of the $|z\rangle$ and $|y\rangle$ states were shifted by about $\pm 18.8 \text{ kHz}$. We used the same Raman frequencies as described earlier and therefore the change in the $|xyz\rangle$ state eigenenergies corresponded to non-zero δ_z and δ_y in Equation 8.8. We chose the detuning such that the initial state had a large overlap with either the $n = 1$ or the $n = 3$ eigenstates of Equation 8.8. We then ramped on the Raman coupling in $750 \mu\text{s}$, adiabatically

mapping the $|z\rangle$ and $|y\rangle$ states into the $n = 1$ or $n = 3$ eigenstates. Because our only experimental knob for dynamically changing the detuning was Ω_{RF} we could not control δ_x so when we initialized the system in $|x\rangle$ the final dressed state always corresponded to the $n = 2$ branch. After turning on the Raman we ramped Ω_{RF} to its final value in 1 ms, effectively ramping δ_z and δ_y close to zero. This detuning ramp had the additional effect of moving the location Dirac point through the atoms when loaded in the $n = 1$ branch, thereby creating a trajectory where the state preparation was not adiabatic. This trajectory depended on the sign of the detuning ramp so we combined data from different initial states in order to exclude the Dirac point trajectories. Near the final location of the Dirac point the state preparation can not be adiabatic regardless of the initial state or detuning used for the ground state preparation. Figure 14a shows an example an absorption image of atoms initially prepared in the $|y\rangle$ state and with δ_y such atoms are loaded in the $n = 1$ branch. The Dirac point is initially located near the lower left edge of the cloud and when δ_i was ramped the location of the Dirac point was dragged across the whole cloud leaving lines where non-adiabatic transitions occurred as can be seen in Figure 14b. The location of the Dirac point as a function of δ_i can also be directly computed by numerically diagonalizing the SOC Hamiltonian from Equation 8.8. At the end of this stage, excluding the points of non-adiabatic transitions, the state of the system was described by the eigenstates in Equation 8.9.

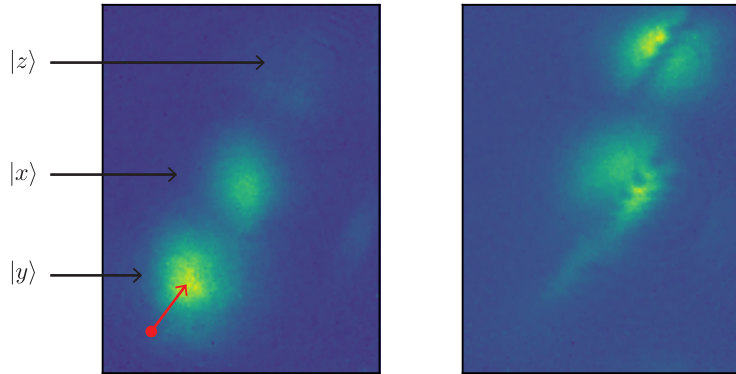


Figure 14: **a** We prepared atoms in the $|y\rangle$ state such that they are adiabatically mapped to the ground dispersion branch. **b** We ramped δ_i and dragged the Dirac point through the atoms.

Free evolution: We suddenly turned off the Raman coupling, thereby projecting the Raman dressed states back into the $|xyz\rangle$ basis. Each of the $|xyz\rangle$ state represents a different branch of the interferometer and they acquire phases that are proportional to t_{free}

$$|\Psi_n(\mathbf{q})\rangle \rightarrow \sum_{j \in xyz} \sqrt{a_{n,j}(\mathbf{q})} e^{i\phi_{n,j}(\mathbf{q})} e^{-iE_j(\mathbf{q})t_{\text{free}}/\hbar} |j, \mathbf{k} = \mathbf{q} - \mathbf{k}_j\rangle, \quad (8.14)$$

where $E_j(\mathbf{q}) = \hbar^2 \mathbf{q}^2 / 2m$ is the free particle energy. The Rashba wavefunction phases $\phi_{n,j}(\mathbf{q})$ that we were interested in measuring were imprinted during the loading procedure. The dynamical phases $E_j(\mathbf{q})t_{\text{free}}/\hbar$ acquired in the different interferometer arms does not contribute to our knowledge of the Rashba eigenstates as they describe the evolution of the system in the absence of Raman dressing.

Recombination pulse: We applied a 25 μs Raman pulse that acted as a second beam splitter in our interferometer sequence. The wave function after the pulse is

$$|\Psi(\mathbf{q})\rangle = \sum_{j,j' \in xyz} \sqrt{a_{n,j}(\mathbf{q})} e^{i(\phi_{n,j}(\mathbf{q}) - E_j(\mathbf{q})t_{\text{free}}/\hbar)} U_{j,j'}(\mathbf{q}) |j, \mathbf{k} = \mathbf{q} - \mathbf{k}_j\rangle, \quad (8.15)$$

where $U_{j,j'}(\mathbf{q}) = |U_{j,j'}(\mathbf{q})| \exp(i\phi_{j,j'}^{(\text{pulse})}(\mathbf{q}))$ is the matrix element of the unitary transformation $\exp(i\hat{H}_{\text{R}}(\mathbf{q})t_{\text{pulse}})$ associated to the Raman pulse. At the end of this procedure, the population in a final state $|l, \mathbf{q}\rangle$ is

$$P_l(\mathbf{q}, t) = \sum_{i \neq j} |U_{l,i}| |U_{j,l}| \sqrt{a_{n,i} a_{n,j}} \cos(\omega_{i,j}(\mathbf{q})t + \phi_{n,i}(\mathbf{q}) - \phi_{n,j}(\mathbf{q}) + \phi_{l,i,j}^{(\text{pulse})}(\mathbf{q})), \quad (8.16)$$

which directly reads out the phase differences, independent of the output port l . Here $\phi_{l,i,j}^{(\text{pulse})}(\mathbf{q})$ is a smoothly varying phase imprinted by the recombination pulse and is independent of \mathbf{q} in the limit of short, strong pulses and does not affect the topological index of the system. The angular frequencies

$$\omega_{i,j}(\mathbf{q}) = \hbar \mathbf{q} \cdot \mathbf{k}_{i,j} / m + \delta_{i,j} \quad (8.17)$$

result from the known free particle kinetic energy, the recoil momenta and detuning $\delta_{i,j}$ from the tripod resonance condition. Figure 13b shows the momentum-dependent populations in each output port at fixed $t_{\text{free}} = 160 \mu\text{s}$ and Figure 13c shows the populations as a function of t_{free} for a representative quasimomentum state $(q_1, q_2) = (0.55, -0.92) k_{\text{L}}$.

We obtained the relative phases $\Delta\phi_{n,i,j,l}(\mathbf{q}) = \phi_{n,i}(\mathbf{q}) - \phi_{n,j}(\mathbf{q}) + \phi_{l,i,j}^{(\text{pulse})}(\mathbf{q})$ from Equation 8.16 by fitting the measured populations to the sum of three cosines with the known free particle frequencies but unknown amplitudes and phases.

8.5.2 Combining phases from different measurements

We combined the phases $\Delta\phi_{n,i,j,l}(\mathbf{q})$ obtained from fits to six different states (two initial states split into 3 states). Similar to the Fourier spectroscopy measurements, we performed a weighted average of the fitted relative phases

$$\Delta\phi_{n,i,j}(\mathbf{q}) = \frac{\sum_l \Delta\phi_{n,i,j,l}(\mathbf{q}) w_{i,j,l}(\mathbf{q})}{\sum_l w_{i,j,l}(\mathbf{q})}, \quad (8.18)$$

where the weights are determined using fit uncertainties and when loading atoms in the topological branch we additionally accounted for the trajectory of the Dirac point

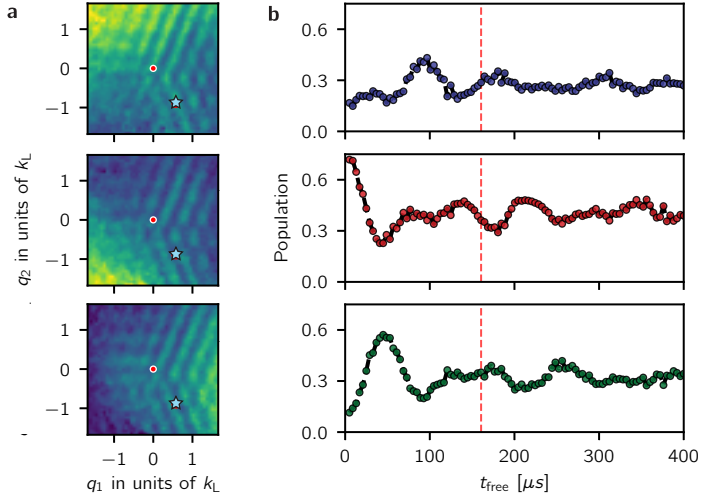


Figure 15: **a** Probabilities as a function of quasimomentum for the three output ports of the interferometer at $t_{\text{free}} = 160 \mu\text{s}$ **b** Probabilities as a function of free evolution time t_{free} for an input state with quasimomentum $(q_1, q_2) = (0.55, -0.92) k_L$ indicated by the blue star on **a** and in the topological ground branch ($n = 1$)

during the loading procedure. Figure 16 shows an example of two different weight arrays used to combine the phase difference associated to the $z \rightarrow x$ transition $i, j = z, x$ for the topological branch $n = 1$ ($\Delta_{1,z,x}$):

The ‘spokes’ in the weight arrays correspond to high uncertainty regions. This uncertainty comes of our inability to resolve the phases of low frequencies $\omega_{ij}(\mathbf{q})$ as well as when two different frequencies $\omega_{ij}(\mathbf{q})$ and $\omega_{i'j'}(\mathbf{q})$ are close to each other which is limited by the largest value of t_{free} in the experiment. I fit and combined a total of 120,000 different time traces (60,000 for each dispersion branch) to produce phase maps like those shown in Figure 17a.

8.5.3 Measuring the topological index

Figure 17a shows typical phase-maps for both the non-topological and topological branches. In the non-topological phase-maps the momentum dependence of the recombination pulse $\phi_{l,i,j}^p(\mathbf{q})$ causes a smooth variation of the phases along the Raman recoil axes that does not affect the evaluation topological index of our system. We recovered the phases $\phi_{n,j}$ of the full spinor wave function from the relative phases $\Delta\phi_{n,i,j}(\mathbf{q})$ by choosing a particular gauge such that $\phi_{n,3} = 0$. We then used the values of $a_{n,i}$ obtained from measuring the populations in the $|xyz\rangle$ states at $t_{\text{free}} = 0$ in combination with the phases of the wave function to compute the Berry connection [117]. Figure 17b shows the three phase differences as a function of polar angle for a loop of radius $q \approx 0.77 k_L$. In addition to the smooth variations induced by the recombination which are present in both columns, the phases of the topological branch have two π valued jumps that lead to non-zero Berry phases when the

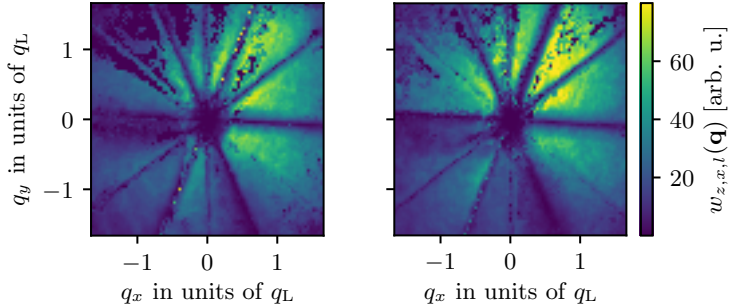


Figure 16: Two sample weight arrays $w_{i,j,l}(\mathbf{q})$ for $i, j = z, x$ and atoms prepared in the topological disperion branch. We obtained the weights using the uncertainties from the fits and the trajectory of the Dirac point during the state preparation. We combined the weights and the phase differences $\Delta\phi_{n,i,j,l}$ obtained from the time dependent fits using Equation 8.18 to obtain the phase maps displayed in Figure 17a

Berry connection is integrated along a closed loop in momentum space. Figure 17c shows the integrated Berry phase as a function of loop radius. As mentioned earlier the largest value of t_{free} limits how well we can resolve the phases of small frequencies and this is reflected in the large variation in the Berry phase depicted in the shaded region of Figure 17c near $q = 0$. For loops with $q > 0.4 k_L$ we obtain an integrated Berry phase that suggests an asymptotic Chern number of $\Phi_B/2\pi = 0.01(1)$ for the non-topological branch and $\Phi_B/2\pi = 0.5(5)$ for the topological branch. However, Berry's phase measurements including ours includes the (potential) contribution of any Dirac strings traversing the integration area. In our system, these are possible at the Dirac point *, and each contributes $\pm 2\pi$ to Φ_B as was discussed in Section 7.6. Even with this 2π ambiguity we are able to associate a half-integer Chern number with the topological branch, which is possible only for a topological dispersion branch in the continuum.

8.6 Conclusion

In conventional lattices — for example graphene, or the topological Haldane model — it is well established that Dirac points each contribute a Berry's phase of $\Phi_B/2\pi = \pm 1/2$ [118], but crystalline materials conspire for these to appear in pairs [119], always delivering integer Chern numbers. In contrast, our continuum system contains a single Dirac point, resulting in a non-integer Chern number. This leads to intriguing questions about edge states at interfaces with non-integer Chern numbers with non-integer Chern number differences. Initial studies in the context of electromagnetic waveguides [120] and atmospheric waves [77] have applied Chern invariants and the bulk-edge correspondence to continuous media.

While the true Rashba Hamiltonian features a ring of degenerate eigenstates, our implementation including the quadratic and cubic Dresselhaus-like SOC lifts

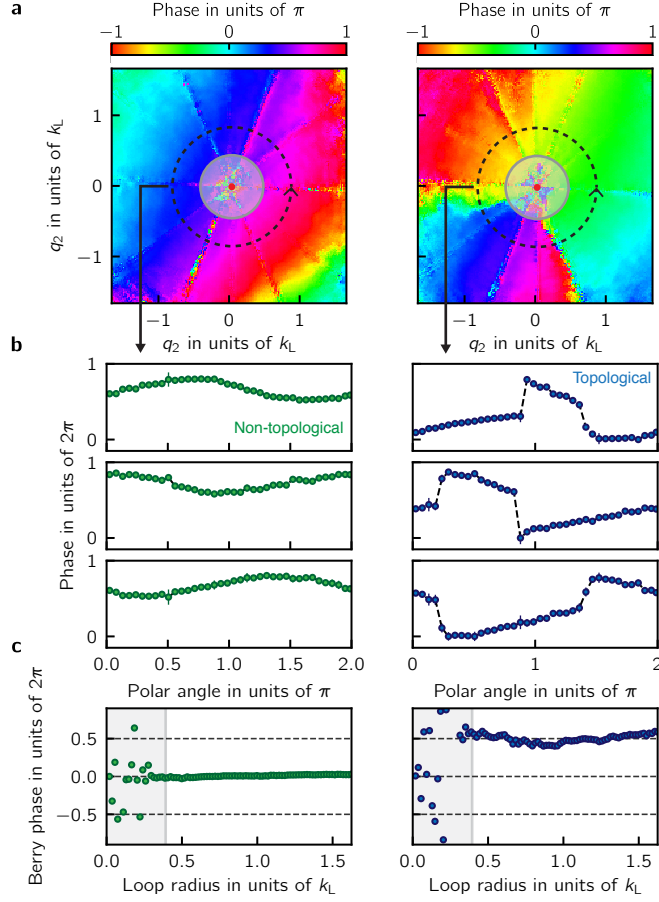


Figure 17: Topological invariants from quantum state tomography, for the non-topological branch ($n = 3$, left) and the topological branch ($n = 1$, right). **a** Phase differences as a function of quasimomentum from the the $z \rightarrow x$ transition **b** Phase differences as a function of polar angle for a loop radius $0.77 k_L$ from the $z \rightarrow x$ (top), $x \rightarrow y$ (middle) and $y \rightarrow z$ (bottom) transitions. The phases associated to the topological branch are characterized by two π valued discontinuities. Each row of phases was shifted by a constant value so that the three rows of phases share the same vertical axis. All phases shown here were binned and averaged using the fit uncertainties as weights. **c** Inferred Chern number as a function of loop radius. For loops with $q > 0.4 k_L$ we obtained an integrated Berry phase and asymptotic Chern number of $\Phi_B/2\pi = 0.01(1)$ for the non-topological branch and $\Phi_B/2\pi = 0.5(5)$ for the topological branch.

this macroscopic degeneracy giving three nearly degenerate minima [108]. Already these three minima could allow the study of rich ground state physics in many body systems of bosons, for example the formation of fragmented BECs [104] when the system does not condense into a single-particle state. Furthermore, the use of additional spin states or larger Raman couplings can partially restore this degeneracy allowing the possible realization of fractional Hall like states [121].